THE JOURNAL OF PHYSICAL CHEMISTRY A

Subscriber access provided by UNIV OF DURHAM

A: New Tools and Methods in Experiment and Theory

Discerning the Contribution of Morphology and Chemistry in Wettability Studies

Karen Sloyan, Chia-Yun Lai, Jin-You Lu, Boulos Alfakes, Saeed M. Alhassan, Ibraheem Almansouri, Marcus Dahlem, and Matteo Chiesa

J. Phys. Chem. A, **Just Accepted Manuscript** • DOI: 10.1021/acs.jpca.8b04197 • Publication Date (Web): 15 Jul 2018

ACS Publications

is published by the American Chemical Society. 1155 Sixteenth Street N.W., Washington, DC 20036

Discerning the Contribution of Morphology and Chemistry in Wettability Studies

Karen Sloyan, Chia-Yun Lai, Jin-You Lu, Boulos Alfakes, Saeed Al Hassan, Ibraheem Almansouri, Marcus S. Dahlem, Matteo Chiesa*

Laboratory for Energy and Nano-Sciences, Khalifa University of Science and Technology, Abu Dhabi, United Arab Emirates.

The wetting behavior of homogeneous systems is now well understood at the macroscopic scale. However, this understanding offers little predictive power regarding wettability when mesoscopic chemical and morphological heterogeneities come to play. The fundamental interest in the effect of heterogeneity on wettability is derived from its high technological relevance in several industries, including the petroleum industry where wettability is recognized as a key determinant of the overall efficiency of the water-flooding based enhanced oil recovery process. Here, we demonstrate the use of the atomic force microscopy force curve measurements to distinguish the roles of chemistry and morphology in the wetting properties of rock formations; thus providing a clear interpretation, and deeper insight on the wetting behavior of heterogeneous formations. Density functional theory calculations further prove the versatility of our approach by establishing benchmarks on ideal surfaces that differ in chemistry and morphology in a predefined manner.

Corresponding Author

*Email: mchiesa@masdar.ac.ae

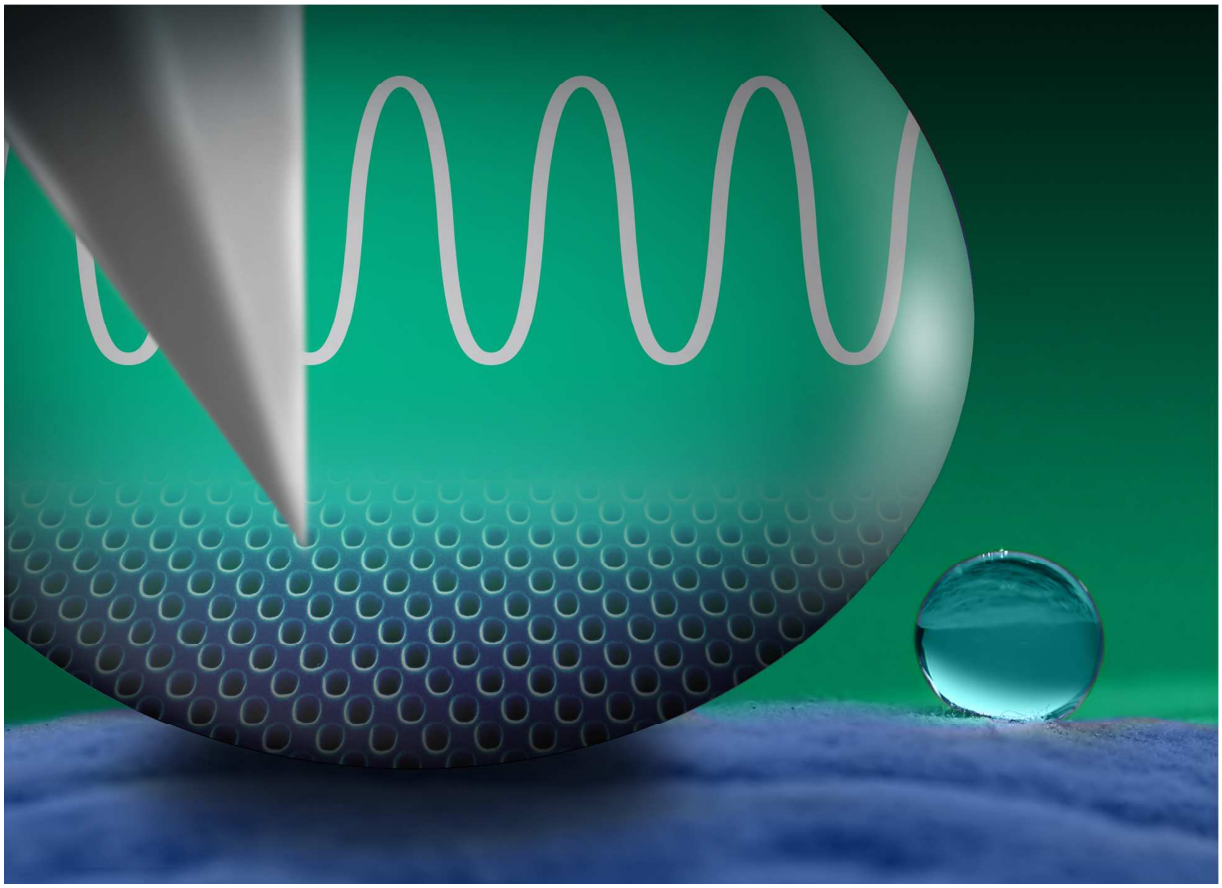

Introduction

Designing and controlling wetting processes at the macroscopic scale has great practical consequences due to their relevance for several industrial applications. Wettability studies often involve the measurement of contact angles as the primary data – a parameter that indicates the degree of wetting when a liquid comes in contact with a solid surface. On an ideal solid surface (flat, rigid, chemical homogeneous, nonreactive, and insoluble), the equilibrium contact angle describes univocally the minimal Gibbs energy of the solid/drop system. In the case of rough

surfaces, however, the Gibbs energy of the system is described by an extra variable *f*, in addition to the apparent contact angle, θ. Despite its intricacy, the extrema conditions of the Gibbs energy fully describe the degree of wetting. Wenzel[1] and Cassie and Baxter[2] established the basis for studying equilibrium wetting on rough hydrophobic surfaces many years ago by simplifying the effort of thermodynamically modeling the entire system and providing equations that yields an apparent contact angle describing the wetting state. When the drop is sufficiently large, in comparison to the typical roughness scale, both the Wenzel and Cassie, and Baxter equations are applicable[3]. However, these equations fail in providing an accurate model of the wetting behavior where chemical heterogeneity also plays an important role in micro scale wettability. The situation is similar from an experimental perspective; while classical static contact angle (SCA), dynamic contact angle (DCA) and nuclear magnetic resonance (NMR) have been demonstrated to be useful as macroscopic techniques[4-6], they all fail at discerning the different role played by morphology and chemistry at the micro scale. This is inherently due to the lack of spatial resolution, in traditional methods, necessary to discern the role of chemistry and morphology.

Perusing the abundant literature in the field of water-flooding based enhanced oil recovery (EOR), dominantly for sandstone-like reservoirs, the reservoir's wetting properties can be easily highlighted as the single most important factor affecting the success of water flooding processes[7]. Thus, it comes as no surprise that the influence of wettability on the efficiency of this process has been studied extensively as documented by many observers[7-12]. Unfortunately, despite the recognition of the fundamental role that wettability plays in this process[7-9, 11-12], the field still lacks a satisfactory understanding of the wettability and its role in oil recovery. The key features that have to be considered in deciphering this problem are related to the physical morphology

and chemical composition of the core – since both of these factors influence the behavior of a particular reservoir and determine the relative permeability and distribution of fluids inside it.

The present study aims to fill this gap by investigating the wetting properties of well-defined macroscopic surfaces, i.e. periodically staggered and flat, by means of a combination of water static contact angle (WCA) and a recently developed dynamic atomic force microscopy (AFM) technique[13-14]. We demonstrate how the interpretation of AFM observables provides an alternative view of wettability with nanoscale resolution. This allows probing the effect of chemistry on wettability and directly decoupling it from roughness above the characteristic size of the probe. As a benchmark, we apply our experimental approach to investigate the effect of water spreading on a set of surfaces of different materials with and without a predefined pattern monster. The observations on the flat surfaces were corroborated by an approach that combines density-functional theory (DFT)-based calculations with a silicon tip in a quasi-static movement y and allows direct comparison with AFM results.

Results and Discussion

The submicron pores of reservoir rocks were represented in our controlled laboratory investigation by fabricating idealized periodic staggered structures on Si by means of e-beam lithography. The process is optimized to consistently create self-similar, repeatable pore dimension structures (details are presented in the Materials and Methods section). The structure consists of pores of a diameter of approximately 180 nm, arranged in a two-dimensional square lattice, with a lattice constant of 510 nm and 270 nm. The porous structure is depicted in Figure

1a). The characteristic depth of the pores is around 120 nm as shown in Figure 1b). The patterned area extends over 1.4 * 1.4 mm^2.

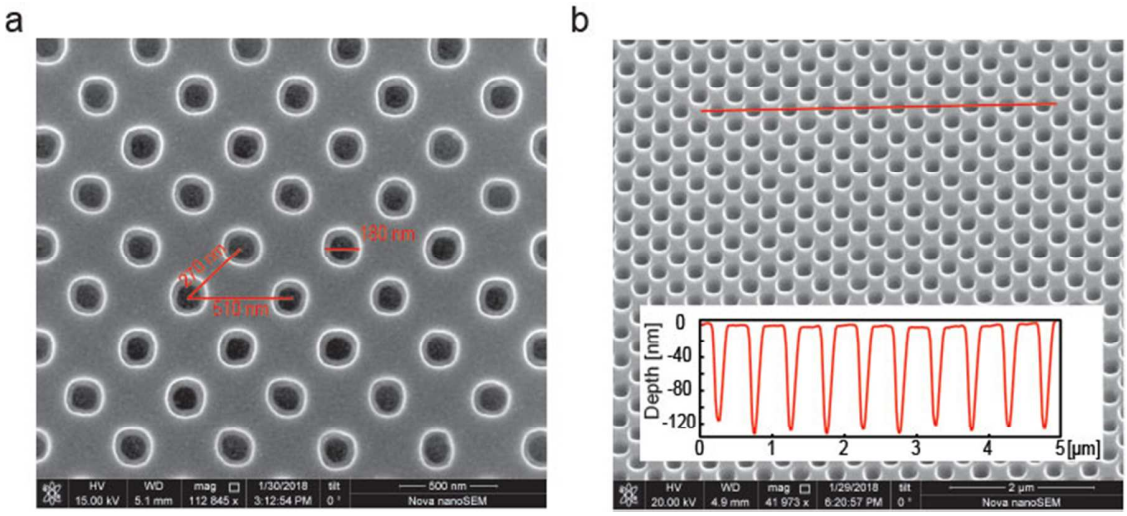

Figure 1. a) A two-dimensional square lattice of pores on a Si substrate is manufactured. The characteristic diameter is approximately 180 nm and lattice constant are 510 nm and 270 nm. b) AFM scans of the surface guarantee the repeatability of the process employed and indicate a characteristic pore depth of approximately 120 nm.

We modify the chemistry of this predefined pattern of Si substrate by a) coating it with a 30 nm SiO_2 layer and b) silane-functionalization. The SiO_2 layer was deposited by means of atomic layer deposition to guarantee a uniform coverage within and inside the pores. Details can be found in the Materials and Methods section.

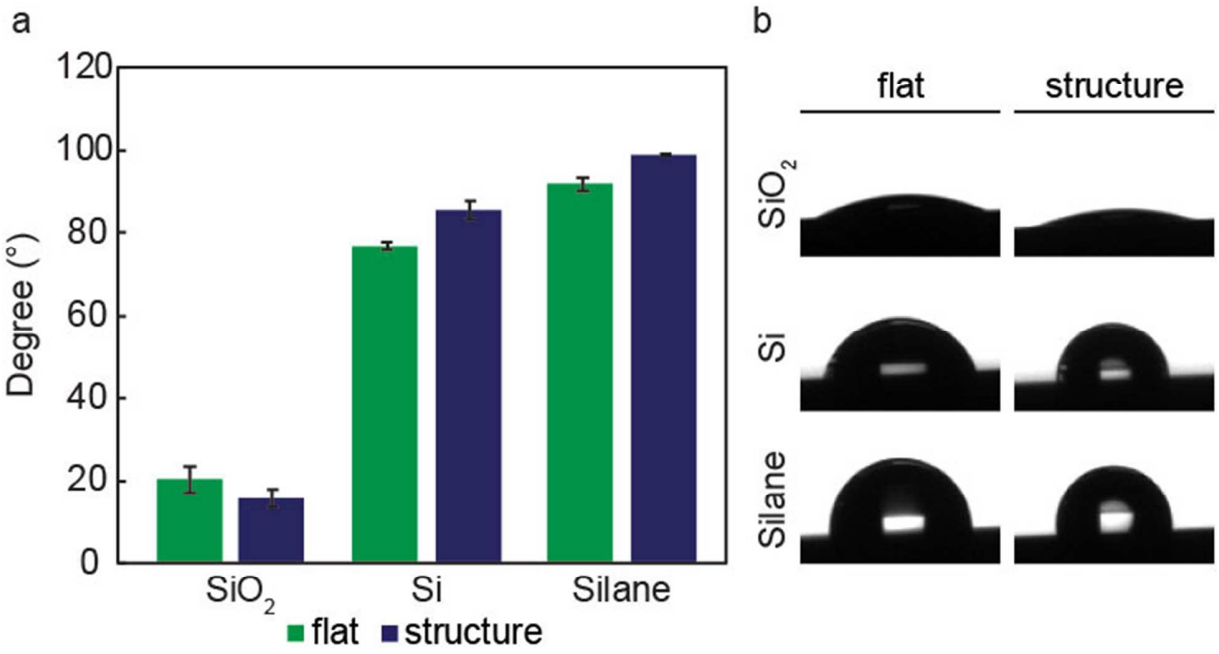

Figure 2. a) Average values for static contact angles of a 1 µl DI water droplet. b) Photograph of the spreading of the 1 µl DI water placed on flat and periodically staggered (structure) SiO_2, Si and silane functionalized substrates.

For the wettability experiments on structures with different chemistry, a sufficiently small water droplet volume, *i.e.,* 1 µl, was chosen so that any spreading is fully contained within the 1.4 × 1.4 mm^2 area of the periodic staggered structure when investigating the patterned structure, see Figure 2b). Despite the small size, the drop is sufficiently large compared with the characteristic length scales of the periodic structure. In order to minimize evaporation of the 1 µl of de-ionized (DI) water and guarantee experimental repeatability, the experiment was carried out at condition close to saturated vapor. Figure 2 shows the WCA collected on flat and patterned surfaces of SiO_2, Si, and silane functionalized substrates. The WCA on the flat surfaces are in line with previously reported data[15-16], which reads 24.1±3.0º, 76.7±0.9º, and 91.7±1.5º for SiO_2, Si, and silane functionalized Si substrate respectively. As for the WCA on the periodic staggered structure surface, 14.1±1.1º, 85.5±2.3º, and 98.9±0.2º were obtained for SiO_2, Si, and silane functionalized

Si substrate. All the numbers reported in this work are averages of 30 droplets over 5 different samples (6 droplets for each sample) to show the repeatability of the WCA measurements. The absolute difference between the WCA of the flat and the patterned structure are examined with Wenzel or Cassie-Baxter models. The well-known expression of Wenzel[1] and Cassie-Baxter[2] reads:

$$\cos\theta_a = r\cos\theta_Y \cdots \text{Wenzel model} \quad (1)$$

$$\cos\theta_a = r_w f\cos\theta_Y + f - 1 \cdots \text{Cassie} - \text{Baxter model} \quad (2)$$

where θ_a is the measured contact angle, θ_Y is the contact angle on an ideal surface, r is the roughness ratio, r_w is the roughness ratio of the wetted area and f is the fraction of the wetted area. Here we used the values of WCA on the flat surfaces for θ_Y, 1.078 for r, 1.003 for r_w, and 0.868 for f. The latter three numbers were obtained from AFM imaging analysis. Applying the Wenzel model for the SiO_2 sample and the Cassie-Baxter model to the Si and silane functionalized Si substrate, the calculated θ_a for SiO_2, Si, and silane functionalized Si substrate is 10.2º, 86.1º, and 99.0º, which is very close to the experimentally obtained WCA on the periodic staggered structure. All the WCA values are summarized in Table I. In this study, this was purposefully engineered in order to point out that the WCA yield information on both morphology and chemistry of the sample.

To decouple the role of chemistry and from morphology, we exploit a method based on the interpretation of the Force (F) versus distance (d) profiles obtained by means of a dynamic atomic force microscopy (AFM) technique. F-d profiles provide the information of van der Waal force field exerted by the sample surface. F-d profiles on flat and periodically staggered structures on SiO_2, Si, and silane functionalized Si substrates are reported in Figure 3a). Each

presented curve is an average of 200 measurements taken at 5 different points on each sample. Student's T-test showed there is no significant difference between flat and structured regions of each sample and significant difference across different samples. By simply comparing the shape of the profile, the F-d profiles on flat and periodically staggered structures are identical. One can explain this outcome by noting that the AFM probe tip radius (~10 nm) is at least one order of magnitude smaller than the characteristic length scales of the periodic structure (~200 nm) making the probe unaffected by the morphology of the surface. Furthermore, this outcome also indicates that by disregarding the morphology factor of the surface, the AFM probe senses the same chemistry on the flat and periodic staggered surfaces, a conclusion that cannot be drawn with macroscopic measurements due to spatial limitation.

Next, by using the sphere-plane model, we further establish a relationship between the absolute values of the force of adhesion F_{AD}, i.e., the minimum of F(d), and the surface energy γ for the flat and periodically staggered structures[17-18]:

$$|F_{AD}| = 4\pi R\gamma \quad (3)$$

where R is the AFM tip radius. As we carefully kept R constant throughout the experiment, it is possible to compare F_{AD} across the samples and we could refer a direct proportionality between F_{AD} and γ. As the values of F_{AD} are identical for the flat and periodically staggered structures within statistical significance, as reported in Figure 3, we clearly confirm that with the spatial resolution ~10 nm, the AFM tip could determine the sole effect of surface chemistry while the macroscopic WCA measurements were affected by the surface roughness.

	SiO_2	Si	Silane
Flat	24.1±3.0º	76.7±0.9º	91.7±1.5º

Periodic staggered	14.1±1.1º	85.5±2.3º	98.9±0.2º
Cassie-Baxter	-	86.1º	99.0º
Wenzel	10.2º	-	-

Table I. WCA on flat and periodic staggered SiO_2, Si, and silane functionalized Si substrates. Water contact angles are also calculated from the Cassie-Baxter and Wenzel models.

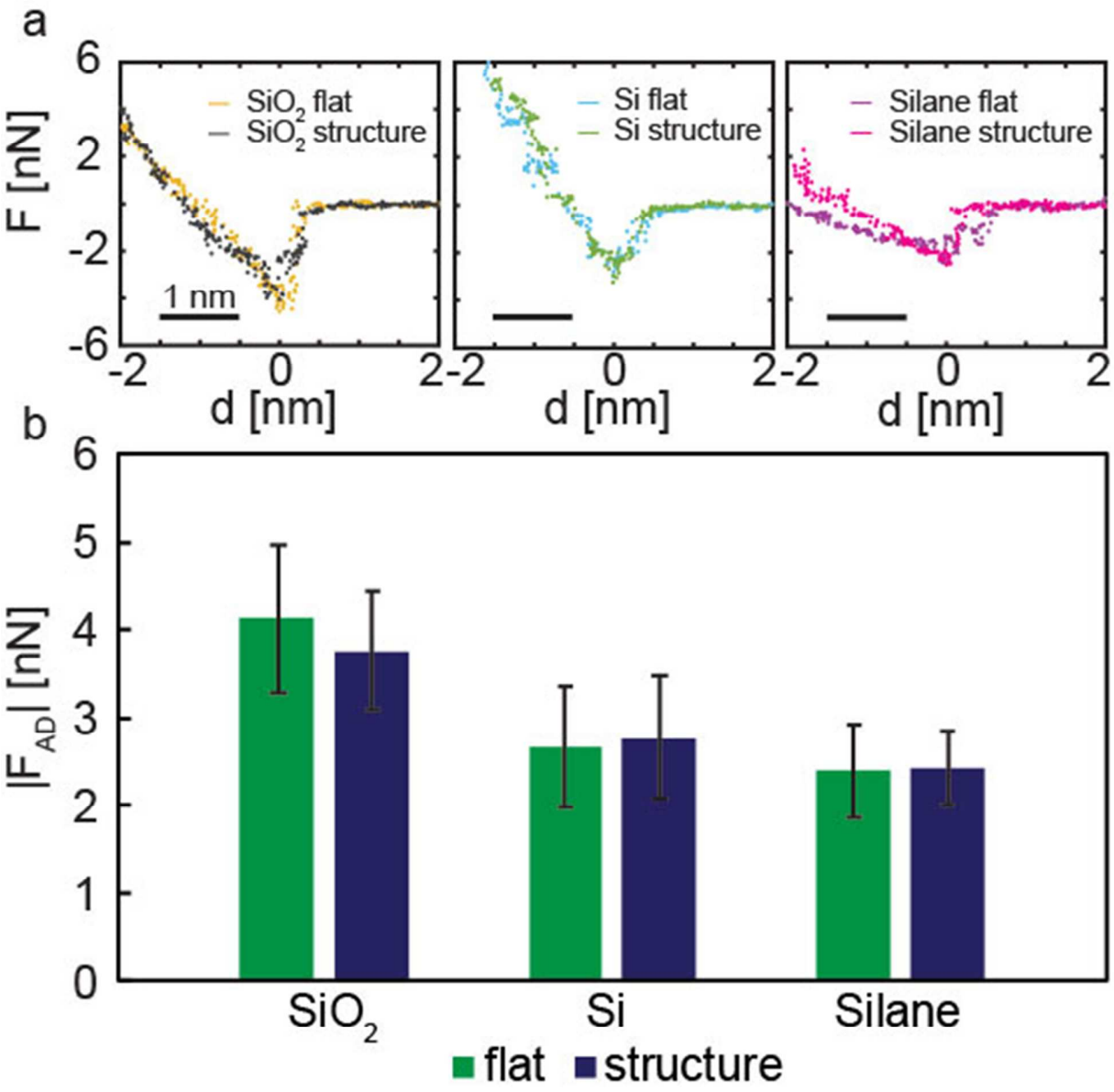

Figure 3. a) F versus d profiles on flat and periodically staggered structures on SiO2, Si, and silane functionalized substrates. b) The absolute value of the force of adhesion F_{AD} for the flat and periodically staggered structures in all

the samples is within the standard deviation of the experiment indicating that the AFM tip is unaffected by morphology.

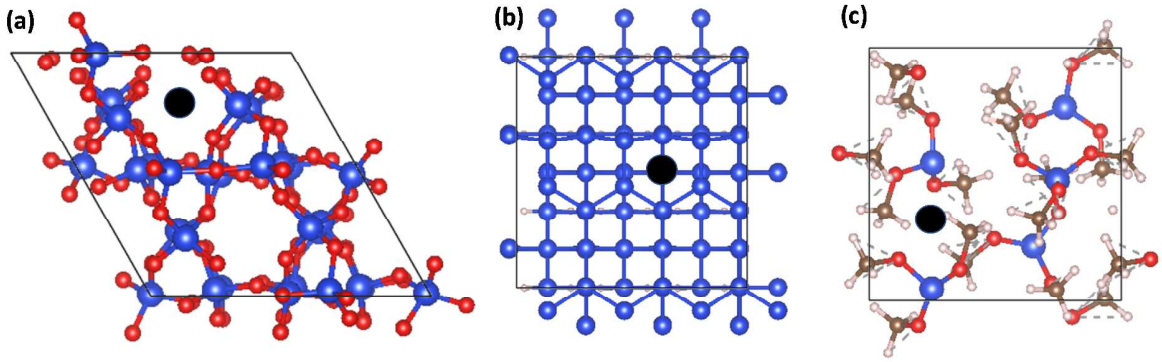

Figure 4. a-c) Top view of configurations of SiO_2, Si, and silane surfaces, respectively. The black point indicates the position of the silicon tip.

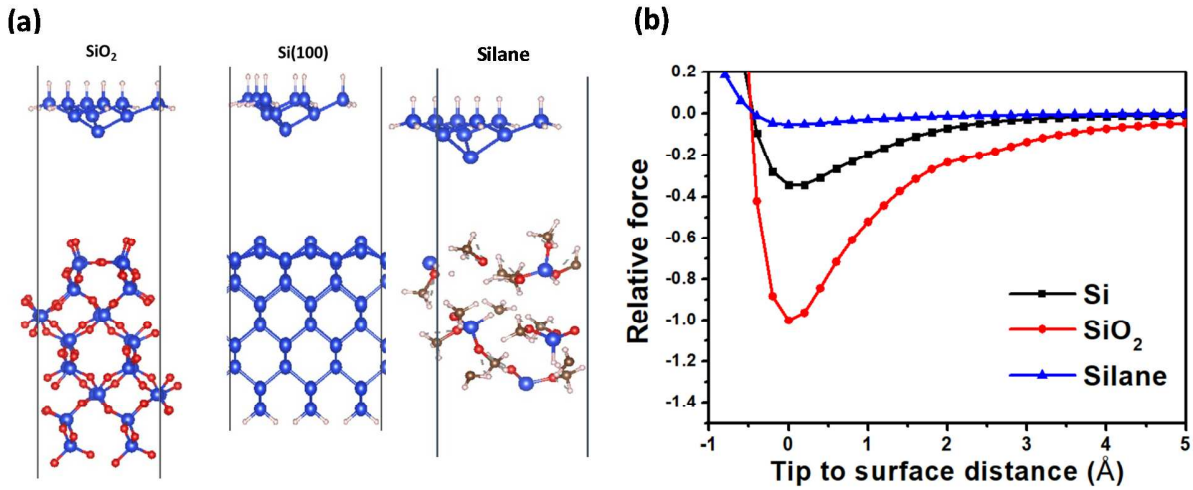

Figure 5. a) Configurations of silicon tip to SiO_2, Si, and silane surfaces, respectively. The Si atoms and H atoms are blue and white spheres, respectively. Other atoms shown with golden carbon and red oxygen. b) DFT predicted force profiles of silicon tip to SiO_2, Si, and, silane surfaces.

To compare the experimental force profiles of the SiO_2, Si, and silane surfaces, we performed plane-wave density functional theory (DFT) to simulate noncontact AFM scanning with a pyramid silicon tip ($Si_{10}H_{15}$). The silicon face centered cubic crystal with (100) plane is used to represent the silicon wafer with the orientation of 100. However, the silica and silane surfaces are experimentally observed as amorphous and cannot be obtained by directly cleaving the crystal structures. Thus, we employ the classical molecular dynamics simulation with reactive force field potentials[19-20] to generate the initial amorphous surfaces. The amorphous SiO_2 is generated by annealing the oxygen-terminated quartz (0001) plane. The annealed SiO_2 surface is negatively charged owing to the top oxygen atoms with only single Si-O bond, which is similar to that predicted by the reactive molecular dynamics of silicon oxidization[21]. The silane amorphous structure was generated from trimethoxysilane $(CH_3O)_3SiH$ rather than the hexadecyltrimethoxysilane $C_{19}H_{42}O_3Si$ used in our experimental silane coating. The reason for this choice is that it is not practical to include the long-chain alkyl part of hexadecyltrimethoxysilane for the computationally expensive scanning simulation, and thus we use only the trimethoxy part as a basis to create amorphous silane surface by performing reactive molecular dynamics simulation at room temperature. The details of the computational simulations are included in the Material and Methods section.

Figure 4(a-c) shows the top-view of the SiO_2, Si and silane functionalized surfaces in the DFT simulation, respectively. In these views, the black points are the sites that the tip apex is pointed at. During the DFT-AFM scanning, the silicon tip approaches the surfaces from top to bottom, as shown in Figure 5a), in a quasi-static manner, and an interval of 0.2 Å. For each step, only four Si atoms at the tip apex are allowed to be relaxed while fixing the silicon tip base and solid surfaces. The DFT predicted force profiles of three different surfaces (SiO2, Si, and silane)

are shown in Figure 5b). The force profiles are taken from the gradient of the total energy of the tip-surface system, which is given by $F = -\nabla(E_{tot}(d))$. Among these three different surfaces, the predicted adhesion forces of the SiO_2 and silane surfaces are the largest and smallest, respectively, which qualitatively agree with the experimental data. However, when it comes to the relative magnitude of adhesion forces among the SiO_2, Si, and silane surfaces, the theoretical prediction does not provide an accurate estimation. This mismatch mainly comes from the difficulty of representing a true amorphous surface within the DFT limited simulation domain and the impracticality of simulating the full long-chain silane chemistry.

Conclusions

In this study, we have prepared flat and periodically staggered Si surfaces with either SiO_2 coating or silane functionalization. Macroscopic measurements (WCA) and nanoscopic measurements (AFM) were both performed on these different structures (flat and staggered pores) and coatings. Our study confirmed that the WCA method is constrained by its intrinsic spatial resolution limit and hence unable to decouple the effects of morphology and chemistry when characterizing the wettability of surfaces with microscopic roughness. This approach gave ~ 10º difference in WCA on the flat and periodically staggered SiO_2, Si, and silane functionalized surfaces. However, with nanoscopic AFM measurements, it is possible to disregard the surface morphology, probing only the chemistry of the rough solid surface. Certainly, these measurements can be performed on different kinds of rough surfaces, for example, spiral or non-periodic structured surfaces, yet we believe that the same conclusion will be drawn. Furthermore, our experimental AFM results are confirmed with DFT-based AFM simulation owing to the agreement of the surface chemistries on different solid surfaces. In this way our methodology has shown a clear indication that with a higher spatial resolution characterizing technique, the

morphology-chemistry coupling issue that complicates wettability studies could be overcome and can be potentially employed to probe the wettability alteration due to surface chemistry functionalization and the adhesion forces of rough surfaces caused by nanoscale patterning.

Materials and Methods

Periodic staggered structures on Si

E-beam lithography (Raith e-LINE) is employed to create periodic staggered structure on a Si substrate. The sample periodicity is illustrated by means of a 45°-tilted SEM image in Figure 1. The characteristic diameter is approximately 180 nm and lattice constant are 510 nm and 270 nm, respectively. The pore depth is ~120 nm as illustrated by the AFM profile. After dicing a new Si wafer, it was sonicated with acetone and IPA (each step had a duration of 5 min). Subsequently the Si substrate was immersed in DI water to remove any trace of solvent for approximately 1 min. A 30 min annealing at 200°C precedes HMDS spin coating (0 rpm for 20 s (static) and then 3000 rpm for 60 s (dynamic)). PMMA A2 (950K) was used as an e-beam positive resist. After spin coating (3000 rpm for 60 s) and prebaking (softbaking) at 180 °C for 90 s, the resist thickness was measured as 72 nm using a Filmetrics F40-UV reflectometer. The pattern was imprinted on a 1.4 × 1.4 mm^2 area. The feature characteristic depths and lattice constant are reported in Figure 1. In order to obtain the necessary resolution for our ~180 nm diameter features, as well as to reduce the time of the large area patterning an acceleration voltage (EHT) of 25 kV and an aperture size of 20 μm were chosen. The dose and element step size for patterning were optimized to 140 $\mu C/cm^2$ and 10 nm, respectively. After around 2 h patterning, the resist

was developed using MIBK/IPA (1:3) for 30 s, and subsequently rinsed by IPA and DI water for 35 s and 30 s, respectively. Subsequently, the structure was etched by SAMCO RIE-200iP Fluorine using SF_6 (10 sccm) and CF_4 (100 sccm) at 1Pa. The optimized etching time was 55 s, whereas the RF powers for BIAS and ICP were chosen 15 W and 100 W, respectively. A flow of O_2 50 sccm for 2 min was used to remove the hard mask. Lastly, HF-etching (49% for 2 min) was used to remove any trace of native oxides or any kind of residuals from the processes described above.

SiO_2 -coated on flat and on periodic staggered structures on Si

In order to vary the chemistry of the periodically patterned Si samples while maintaining the same morphology, SiO_2 was deposited on the periodic structure created on the Si substrate by means of an Oxford FlexAL Atomic Layer Deposition (ALD) tool at 150°C for 52 mins (200 cycles). BTBAS-t-butylaminosilane and O_2 were employed as precursors, while Ar as a purging gas. Specifically, a deposition cycle consisted of a 3 s pulse of BTBAS precursor, followed by 3 s Ar purge, then a 3 s pulse of 60 sccm of O_2 at 250 W plasma power, followed by a 2 s Ar purge. The pressure was set to 80 Torr during the BTBAS pulse, and to 15 Torr during the plasma O_2 pulse. The SiO_2 layer thickness was measured using a J.A Woollam Variable Angle Ellipsometer, and the results were fitted using a Cauchy model yielding thickness and refractive index of ~30 nm and 1.44, respectively.

$C_{19}H_{42}O_3Si$ –functionalization of flat and periodic staggered structures on Si

“Silanization” of the flat and periodic staggered Si structure was realized by allowing $C_{19}H_{42}O_3Si$ adsorption on the sample in a fume hood. 5 drops of silanization agent ($C_{19}H_{42}O_3Si$) were placed in an aluminum foil cap whereupon the wafer was placed functioning as a seal for

the cap. After 2.5 h, the wafer was placed on a hotplate at 150°C for 10 mins to cure and evaporate the excessive silane.

WCA measurement.

Contact angle measurements were made using a Kruss FM40Mk2 EasyDrop contact angle goniometer. For measurements of the so-called "static" contact angle, we adopted a procedure described by Bain et al.[22-23]. Such procedure consists in bringing a 1 µl DI water drop formed at the end of a needle into contact with the surface. To avoid electrostatic charging, needle and surface were electrically grounded. Once the drop was in contact with the surface, the needle was removed and the contact angle measured by the standard software provided by Kruss. Contact angles were measured from both sides of 6 droplets on each sample, and the mean and standard deviation of these measurements are reported (the typical uncertainty is in the range 1-2°). For reproducibility, we took particular care in avoiding evaporation of the small droplet during our data collection by carrying out the measurement at close to saturated vapor pressure conditions. Data from at least 5 samples of flat and periodic structured SiO_2, Si and silanized-Si were collected to yield statistical validity.

AFM-force measurement.

The AFM data was collected in ambient conditions in standard dynamic AFM[24], *i.e.*, in particular in amplitude modulation AFM, since it allows recovering the full force (F) versus distance (d) profile[13, 25]. In our experiments, the effective radius R was monitored *in-situ* with the use of the critical amplitude A_C method that provides a functional relationship in dynamic AFM between the minimum free amplitude A_0 required to reach the repulsive regime and R, *i.e.* $R=4.75(A_c)^{1.1}$ as reported elsewhere[26] was used here to monitor R throughout the experiments. The amplitude-

phase distance data was converted into force F versus distance d profiles by employing the Sader-Jarvis-Katan formalism[14, 24, 27]. In this formalism, the raw amplitude A ($A \equiv A_1 \equiv A_{sp}$) and phase φ ($\varphi = \varphi_1$) versus separation distance d curves were recorded and comprise the input while the F-d profiles were obtained by means of the Sader-Jarvis-Katan (SJK) formalism:

$$F(d) = 2k\int_{u=d}^{u=\infty}\left[\left(1+\frac{A^{1/2}(u)}{8\sqrt{\pi(u-d)}}\right)\Omega(u) - \frac{A^{3/2}(u)}{\sqrt{2(u-d)}}\frac{d\Omega(u)}{du}\right]du \quad (4)$$

The cantilever-surface separation z_c can relate d_m, or equivalently d, to the oscillation amplitude A by $d_m \equiv d \approx z_c - A$. Ω is the normalized frequency that reads:

$$\Omega(d) = [1+\frac{A_0}{QA}\cos(\Phi(d))]^{\frac{1}{2}} - 1 \quad (5)$$

where A_0 is the free or unperturbed amplitude of oscillation and Φ is the phase lag relative to the drive force. For convention we assign d = 0 when the minima in F occurs, *i.e.*, $F = F_{AD}$, and distances are defined experimentally. The robust use of (4)-(5) requires that the force transitions occur smoothly in AM AFM and that bi-stability is avoided. This is required to recover the force and energy for the whole range of distances including long range and tip-sample deformation. Experimentally, here, the smoothness in the force transitions is achieved by sufficiently increasing the free amplitude A_0 above the critical region of bi-stability[28-29]. For OLYMPUS (AC160TS) cantilevers with k≈30 N/m, Q≈400, and f0≈280 kHz, the smooth transition occurs for values of A_0 larger than 20–30 nm when the tip radius R lies in the 5 to 10 nm range and for Si and SiO_2 samples[26]. A minimum of 200 force profiles is reconstructed on each sample on at least 5 different locations within each sample.

Density functional theory noncontact atomic force simulations.

All DFT noncontact atomic force simulations were performed using the Quantum Espresso package[30]. The potential basis sets in the generalized gradient approximations (GGA) use Perdew Burke Ernzerhof (PBE) functional and ultra-soft pseudopotentials. For van der Waals corrections, the DFT-D2 method of Grimme[31] is applied to the DFT simulations. The kinetic energy cutoffs and density cutoffs are set as 30/240 Ry and the gamma point is used for all the total energy calculations. Silicon pyramid tip ($Si_{10}H_{15}$), amorphous SiO_2, silane and silicon (100) crystal planes are relaxed by DFT geometry optimization before running noncontact atomic force simulations. The criterion for the geometry optimization is met once the total energy is less than 1×10^{-4} Ry and the interatomic force is less than 4×10^{-4} Ry/bohr. The force profiles are directly extracted by taking the gradient of the total energy of the system versus the distance between the silicon tip and solid surface. For comparison purpose, the tip to surface distance was refined by taking the position with the largest attractive force as the origin for the SiO_2, Si, silane surfaces, respectively. For comparison, the force-distance profiles are also normalized by dividing the adhesion force of SiO_2.

In order to have amorphous SiO_2 and silane configurations, we employed a molecule dynamics simulation with a reactive force potential[19]. The SiO_2 surface was generated by annealing the oxygen-terminated quartz (0001) plane at 1500K for 50 pico-seconds with the time step of 1 femto-second and then cooling it down to room temperature. After getting the annealed SiO_2 surface, the configuration was relaxed by performing the DFT geometry optimization. For the silane configuration, the initial configuration was taken from the trimethoxysilane $C_3H_{10}O_3Si$ rather than the hexadecyltrimethoxysilane $C_{19}H_{42}O_3Si$ used in our silane coating. The reason for this is that it is not practical to include the long-chain alkyl part of hexadecyltrimethoxysilane for the computationally expensive scanning simulation, and thus we put the trimethoxy part as a

basis to create amorphous silane surface by performing molecular dynamic simulation at 1500K for 50 pico-seconds.

Acknowledgements

This work was supported in part by the Gas Subcommittee Research and Development under Abu Dhabi National Oil Company (ADNOC).

References

1. Wenzel, R. N., RESISTANCE OF SOLID SURFACES TO WETTING BY WATER. *Industrial & Engineering Chemistry* **1936,** *28* (8), 988-994.
2. Cassie, A. B. D.; Baxter, S., Wettability of porous surfaces. *Transactions of the Faraday Society* **1944,** *40* (0), 546-551.
3. Marmur, A., Wetting on Hydrophobic Rough Surfaces: To Be Heterogeneous or Not To Be? *Langmuir : the ACS journal of surfaces and colloids* **2003,** *19* (20), 8343-8348.
4. Brown, R. J. S.; Fatt, I., Measurements Of Fractional Wettability Of Oil Fields' Rocks By The Nuclear Magnetic Relaxation Method. In *Fall Meeting of the Petroleum Branch of AIME*, Society of Petroleum Engineers: Los Angeles, California, 1956.
5. Abdallah, W.; Buckley, J. S.; Carnegie, A.; Edwards, J.; Herold, B.; Fordham, E.; Graue, A.; Habashy, T.; Seleznev, N.; Signer, C., Fundamentals of wettability. *Tech* **1986,** *38* (1125-1144), 268.
6. Yousef, A. A.; Al-Saleh, S.; Al-Kaabi, A. U.; Al-Jawfi, M. S., Laboratory Investigation of Novel Oil Recovery Method for Carbonate Reservoirs. In *Canadian Unconventional Resources and International Petroleum Conference, 19-21 October*, Society of Petroleum Engineers: Calgary, Alberta, Canada, 2010.
7. Anderson, W. G., Wettability Literature Survey-Part 6: The Effects of Wettability on Waterflooding. *Journal of Petroleum Technology* **1987,** *39* (12), 1605-1622.
8. Craig, F. F., *The reservoir engineering aspects of waterflooding*. Richardson, TX: Henry L. Doherty Memorial Fund of AIME, Society of Petroleum Engineers: 1993.
9. Morrow, N. R.; Lim, H. T.; Ward, J. S., Effect of Crude-Oil-Induced Wettability Changes on Oil Recovery. *SPE Formation Evaluation* **1986,** *1* (01), 89-103.
10. Morrow, N. R., Wettability and Its Effect on Oil Recovery.
11. du Petrole, F.; Malmaison, F. R., Evaluation of reservoir wettability and its effect on oil recovery. In *Interfacial Phenomena in Petroleum Recovery*, CRC Press Boca Raton, FL: 1990; p 319.
12. Karabakal, U.; Bagci, S., Determination of Wettability and Its Effect on Waterflood Performance in Limestone Medium. *Energy Fuels* **2004,** *18* (2), 438-449.
13. Lai, C.-Y.; Tang, T.-C.; Amadei, C. A.; Marsden, A. J.; Verdaguer, A.; Wilson, N.; Chiesa, M., A nanoscopic approach to studying evolution in graphene wettability. *Carbon* **2014,** *80* (0), 784-792.
14. Amadei, C. A.; Santos, S.; Pehkonen, S. O.; Verdaguer, A.; Chiesa, M., Minimal Invasiveness and Spectroscopy-Like Footprints for the Characterization of Heterogeneous Nanoscale Wetting in Ambient Conditions. *The Journal of Physical Chemistry C* **2013,** *117* (40), 20819-20825.

15. Egatz-Gomez, A.; Majithia, R.; Levert, C.; Meissner, K. E., Super-wetting, wafer-sized silicon nanowire surfaces with hierarchical roughness and low defects. *RSC Advances* **2012,** *2* (30), 11472-11480.
16. Shahsavan, H.; Quinn, J.; d'Eon, J.; Zhao, B., Surface modification of polydimethylsiloxane elastomer for stable hydrophilicity, optical transparency and film lubrication. *Colloids Surf. Physicochem. Eng. Aspects* **2015,** *482*, 267-275.
17. Yaminsky, V. V., The hydrophobic force: the constant volume capillary approximation. *Colloids Surf. Physicochem. Eng. Aspects* **1999,** *159* (1), 181-195.
18. Israelachvili, J., *Intermolecular & Surface Forces*. 2 ed.; Academic Press: New York, 1991.
19. Kulkarni, A. D.; Truhlar, D. G.; Goverapet Srinivasan, S.; van Duin, A. C. T.; Norman, P.; Schwartzentruber, T. E., Oxygen Interactions with Silica Surfaces: Coupled Cluster and Density Functional Investigation and the Development of a New ReaxFF Potential. *The Journal of Physical Chemistry C* **2013,** *117* (1), 258-269.
20. *Atomistix ToolKit*, QuantumWise: 2006.
21. Khalilov, U.; Pourtois, G.; Huygh, S.; van Duin, A. C. T.; Neyts, E. C.; Bogaerts, A., New Mechanism for Oxidation of Native Silicon Oxide. *The Journal of Physical Chemistry C* **2013,** *117* (19), 9819-9825.
22. Bain, C. D.; Troughton, E. B.; Tao, Y. T.; Evall, J.; Whitesides, G. M.; Nuzzo, R. G., Formation of monolayer films by the spontaneous assembly of organic thiols from solution onto gold. *J. Am. Chem. Soc.* **1989,** *111* (1), 321-335.
23. Bain, C. D.; Whitesides, G. M., Modeling Organic Surfaces with Self‐Assembled Monolayers. *Angew. Chem.* **1989,** *101* (4), 522-528.
24. Katan, A. J.; van Es, M. H.; Oosterkamp, T. H., Quantitative force versus distance measurements in amplitude modulation AFM: a novel force inversion technique. *Nanotechnology* **2009,** *20* (16), 165703.
25. Santos, S.; Amadei, C. A.; Verdaguer, A.; Chiesa, M., Size Dependent Transitions in Nanoscale Dissipation. *The Journal of Physical Chemistry C* **2013,** *117* (20), 10615-10622.
26. Santos, S.; Guang, L.; Souier, T.; Gadelrab, K.; Chiesa, M.; Thomson, N. H., A method to provide rapid in situ determination of tip radius in dynamic atomic force microscopy. *Review of Scientific Instruments* **2012,** *83* (4), 043707.
27. Sader, J. E.; Jarvis, S. P., Accurate formulas for interaction force and energy in frequency modulation force spectroscopy. *Appl. Phys. Lett.* **2004,** *84* (10), 1801-1803.
28. Sergio, S.; Victor, B.; Josep, F.; Neil, H. T., Cantilever dynamics in amplitude modulation AFM: continuous and discontinuous transitions. *Journal of Physics D: Applied Physics* **2010,** *43* (27), 275401.
29. Santos, S.; Barcons, V.; Font, J.; Thomson, N. H., Bi-stability of amplitude modulation AFM in air: deterministic and stochastic outcomes for imaging biomolecular systems. *Nanotechnology* **2010,** *21* (22), 225710.
30. Paolo, G.; Stefano, B.; Nicola, B.; Matteo, C.; Roberto, C.; Carlo, C.; Davide, C.; Guido, L. C.; Matteo, C.; Ismaila, D.; Andrea Dal, C.; Stefano de, G.; Stefano, F.; Guido, F.; Ralph, G.; Uwe, G.; Christos, G.; Anton, K.; Michele, L.; Layla, M.-S.; Nicola, M.; Francesco, M.; Riccardo, M.; Stefano, P.; Alfredo, P.; Lorenzo, P.; Carlo, S.; Sandro, S.; Gabriele, S.; Ari, P. S.; Alexander, S.; Paolo, U.; Renata, M. W., QUANTUM ESPRESSO: a modular and open-source software project for quantum simulations of materials. *J. Phys.: Condens. Matter* **2009,** *21* (39), 395502.
31. Grimme, S.; Antony, J.; Ehrlich, S.; Krieg, H., A consistent and accurate ab initio parametrization of density functional dispersion correction (DFT-D) for the 94 elements H-Pu. *The Journal of chemical physics* **2010,** *132* (15), 154104.

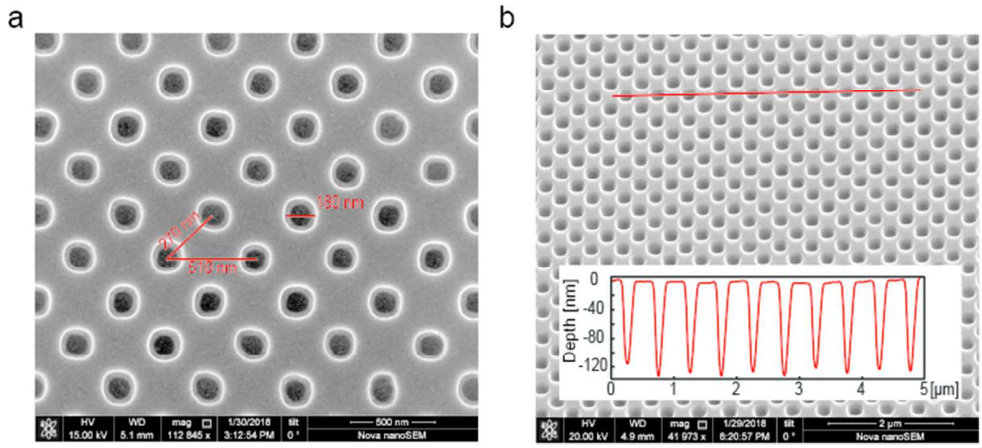

Figure 1

125x57mm (150 x 150 DPI)

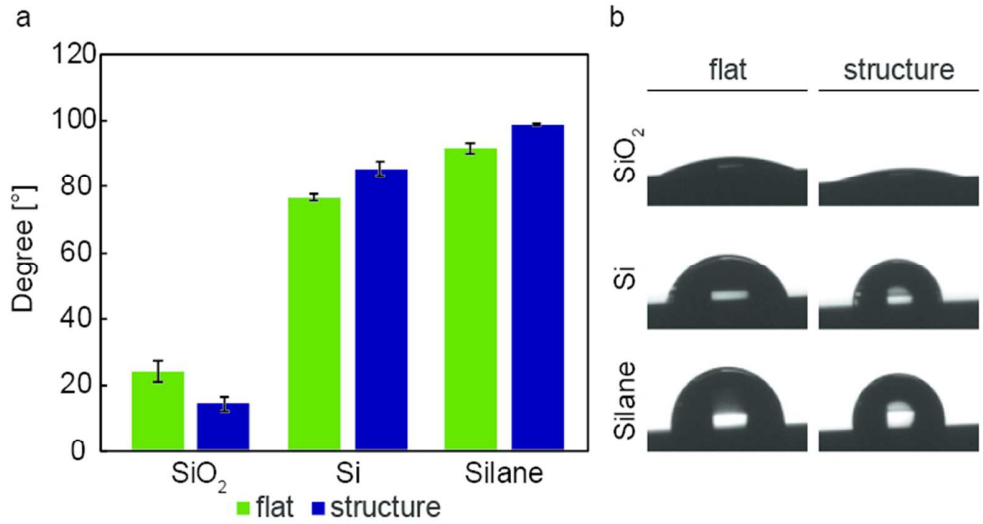

Figure 2

132x71mm (150 x 150 DPI)

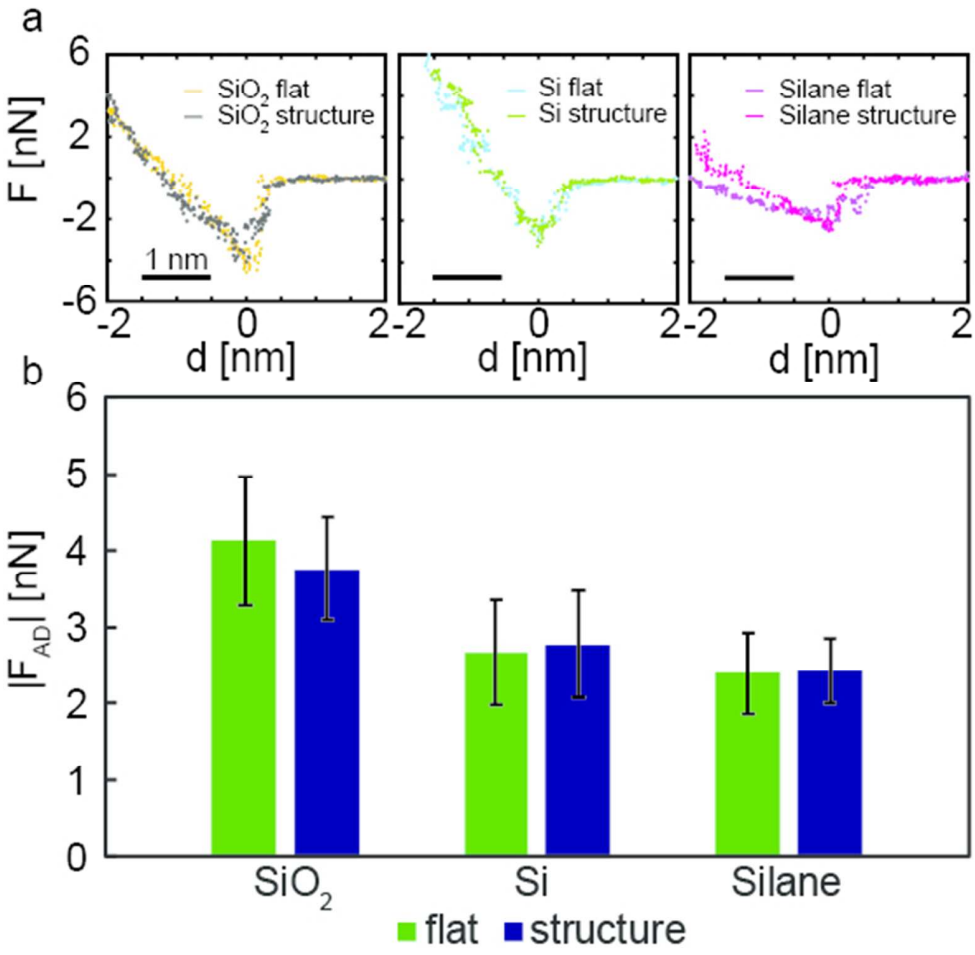

Figure 3

94x93mm (150 x 150 DPI)

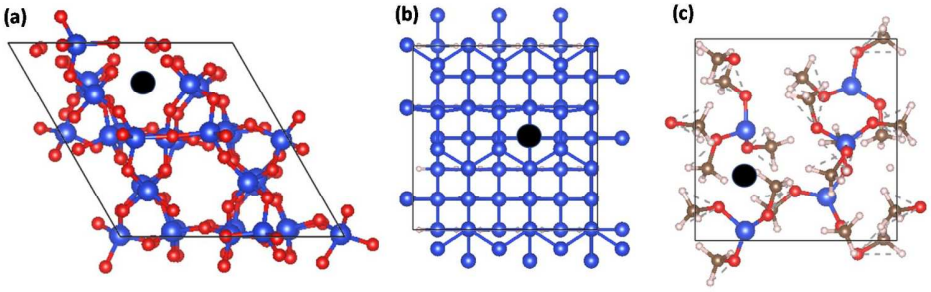

Figure 4

485x155mm (96 x 96 DPI)

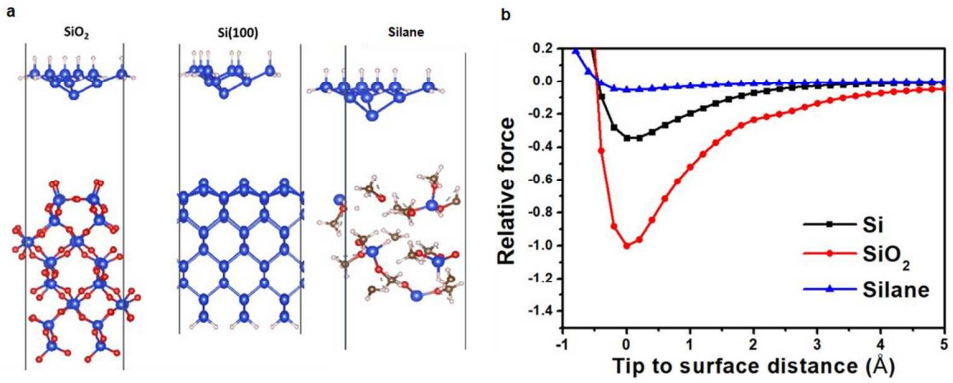

Figure 5

304x124mm (96 x 96 DPI)

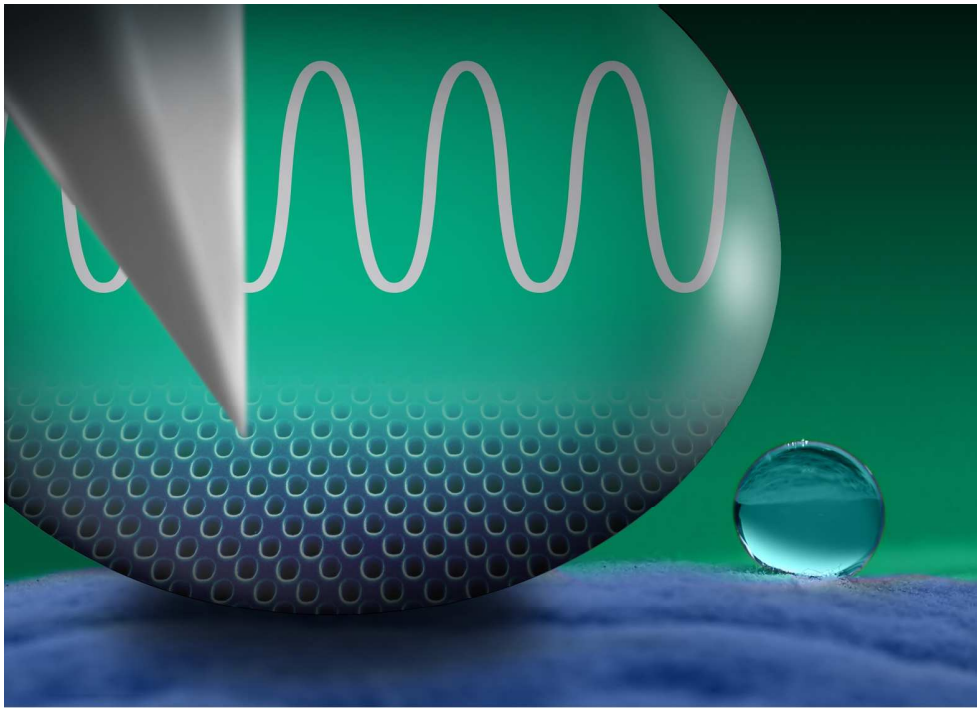

TOC

187x135mm (300 x 300 DPI)